Facile one pot sonochemical synthesis of layered nanostructure of ZnS NPs/rGO nanosheets for simultaneous analysis of daclatasvir and hydroxychloroquine

Saad A. Alkahtani [a], Ashraf M. Mahmoud [b,c], Mater H. Mahnashi [b], Ali O. AlQarni [b], Yahya S. A. Alqahtani [b], Mohamed M. El-Wekil [c,*]

[a] Department of Clinical Pharmacy, College of Pharmacy, Najran University, Najran, Saudi Arabia
[b] Department of Pharmaceutical Chemistry, College of Pharmacy, Najran University, Najran, Saudi Arabia
[c] Department of Pharmaceutical Analytical Chemistry, Faculty of Pharmacy, Assiut University, Assiut, Egypt

ARTICLE INFO

ABSTRACT

In this study, zinc sulfide nanoparticles were loaded on reduced graphene oxide (ZnS NPs/rGO) using simple sonochemical method. The nanocomposite was characterized using different morphological and electrochemical techniques such as TEM, SEM, PXRD, EDX, Raman spectroscopy, FTIR, N_2-adsorption–desorption, CV, and EIS. The ZnS NPs/rGO modified glassy carbon electrode (GCE) was used to simultaneously estimate hydroxychloroquine (HCQ) and daclatasvir (DAC) in a binary mixture for the first time. The modified nanocomposite exhibited good catalytic activity towards HCQ and DAC detection. In addition, it showed higher sensitivity, good selectivity and stability; and high reproducibility towards HCQ and DAC analysis. The activity of the modified electrode was noticeably improved due to synergism between ZnS NPs and rGO. Under optimum conditions of DPV measurements, the anodic peak currents (Ipa) were obviously increased with the increase of HCQ and DAC amounts with linear ranges of 5.0–65.0 and 7.0–65.0 nM with LODs of 0.456 and 0.498 nM for HCQ and DAC, respectively. The ZnS NPs/ rGO modified GCE was used to quantify HCQ and DAC in biological fluids with recoveries of 98.7–102.7% and 96.9–104.5% and RSDs of 1.89–3.57% and 1.91–3.70%, respectively.

1. Introduction

Coronavirus disease 19 (COVID-19) has focused great attention on the urgent need to develop effective therapies against the causative agent, SARS-CoV-2 [1–3]. Daclatasvir (DAC), anti-viral agent, can bind to the replication complex components of 2019-nCoV with an inhibitory potency with Kd of 23.31 nm [4]. Hydroxychloroquine (HCQ) was used as a bioactive agent, and was reported to possess antiviral activities against RNA viruses as hepatitis C virus [5] hepatitis A virus [6] influenza A H5N1 virus [7] Ebola virus [8] as well as DNA viruses such as herpes simplex virus [9] and hepatitis B virus [10]. Recent publications support the hypothesis that HCQ can improve the clinical outcome of patients infected by SARS-CoV-2. Anti-SARS-CoV-1 actions of HCQ in vitro were attributed to a deficit in the glycosylation of a virus cell surface receptor, the angiotensin-converting enzyme 2 (ACE2) on Vero E6 cells [11,12].

Sonochemical technique is an efficient, simple and economic method for synthesis of nanomaterials. It provides shorter reaction times and more energy efficiency with an environmental friendly technique [13,14].

Due to their low cost, plenty of morphologies, good electro-catalytic activity, high surface area and promoting electron transfer, inorganic nanomaterials have attracted more interest as sensors and biosensors [15–21]. Among them, zinc sulfide (ZnS) has been greatly used due to several advantages such as low cost, non-toxic, easily fabricated, high capacitance and good stability [22].

Reduced graphene oxide (rGO) is considered an ideal electrochemical nanomaterial for different applications due to its unique chemical, electrical and optical properties [23–26]. The advantages of rGO are ease of preparation (from graphene oxide), stable dispersion in water and high number of catalytic sites on its surface [27–29]. In addition, rGO interacts with ZnS NPs by the means of electrostatic interactions [30]. Therefore, our approach based on the synthesis of ZnS NPs@ rGO by facile sonochemical method. It is noteworthy to mention

---

that the nanomaterials prepared via ultra-sonication exhibit porous nanostructure and porous structure [31,32]. In addition, the preparations of nanomaterials based on sonochemical approach are free from toxic solvents and easy to manipulate [33–35].

As rationale inspired by these facts, an economic and artful electrochemical nanosensor was proposed for simultaneous voltammetric analysis of daclatasvir (DAC) and hydroxychloroquine (HCQ) in human plasma and urine samples for the first time. The sensor based on the synthesis of zinc sulfide nanoparticles/reduced graphene oxide (ZnS NPs@ rGO) by sonochemical technique. The main advantages of the proposed sensor are simplicity, sensitivity, reliability and selectivity, while the main disadvantage is inability to determine these analytes in presence of chloroquine.

2. Experimental

2.1. Materials and reagents

Daclatasvir was obtained as a gift from NODCAR, El-Dokki, Giza, Egypt. Hydroxychloroquine sulfate, Graphene oxide, hydrazine, uric acid, methionine, cysteine, adenine, guanine, glutathione were purchased from Sigma Aldrich. Glucose, Potassium permanganate, ethanol, sodium nitrate, hydrochloric acid, acetonitrile, ferrocyanide, ferricyanide, boric acid, phosphoric acid, sodium sulfide, zinc chloride were purchased from El-Nasser Intermediate for Chemicals, Cairo, Egypt.

2.2. Instrumentation

Included within Electronic Supplementary Materials (ESM).

2.3. Preparation of human urine and plasma samples

2.5 mL of urine sample (from healthy volunteers) was centrifuged at 1500 rpm for 20 min. Then, the urine sample was filtered using 0.45 mm filter paper and 0.5 mL of the supernatant was transferred to voltammetric sample containing phosphate buffer (pH = 6.0). 0.5 mL Human plasma was mixed with 1.0 mL ACN and subjected to centrifugation to about 30 min to remove possible interference. After that, the supernatant was collected and diluted with 5 mL phosphate buffer (pH = 6.0) prior to the voltammetric analysis [36].

2.4. Sonochemical preparation of ZnS NPs/rGO

Graphite oxide (GO) was synthesized from natural graphite by modified Hummers method. Then, 50 mg of the synthesized GO was dispersed in water and ultrasonicated for 90 min. Then, 0.5 mM of $ZnCl_2$ and 0.25 mM of Na_2S were added to the mixtures under stirring before addition of 30 mL of ethylene glycol. The final mixture was allowed in ultrasonic water bath (50 kHz frequency and 60 W) for 30 min. After that, the final product was centrifuged at 4000 rpm and washed with ethanol and double distilled water before calcination at 650 °C for 3 h under N_2 steam.

2.5. Modification of glassy carbon electrode with ZnS NPs@rGO

250 mg of ZnS@rGO was suspended in 100 mL DDW and sonicated for 20 min. Then, 5 µL of the prepared dispersion (2.5 mg mL^{-1}) was drop casted on the surface of clean GCE (Scheme 1).

3. Results and discussions

3.1. Role of ultrasonic irradiations on the preparation of nanomaterials and detection mechanism

The waves produced by the sonicator generate tiny and highly energetic vapor filled bubbles that upon implosive collapse can create more microjets, locally high temperature and pressure. These formed microbubbles make ZnS NPs to move from the bulk solution to the surfaces of rGO nanosheets. Moreover, the hydrodynamic interaction of microbubbles with the mixed solutions improves the dispersion of nanoparticles on the surface of rGO and prevents their aggregations [37,38]. It was found that the nanoparticles produced by the chemical sonication would have lower particle sizes (25–30 nm) than untreated ones (50–60 nm). Fig. S1 shows the electrochemical oxidation of 40.0 nM DAC and HCQ at ZnS NPs@rGO with and without ultrasonication where the peak currents of DAC and HCQ are higher in the case of nanocomposite treated with ultrasonic irradiations.

3.2. Rationale of the sensor design

Metal sulfides have more interest and considerable attention for its unique properties like chemical stability, low cost, less-toxicity, catalytic
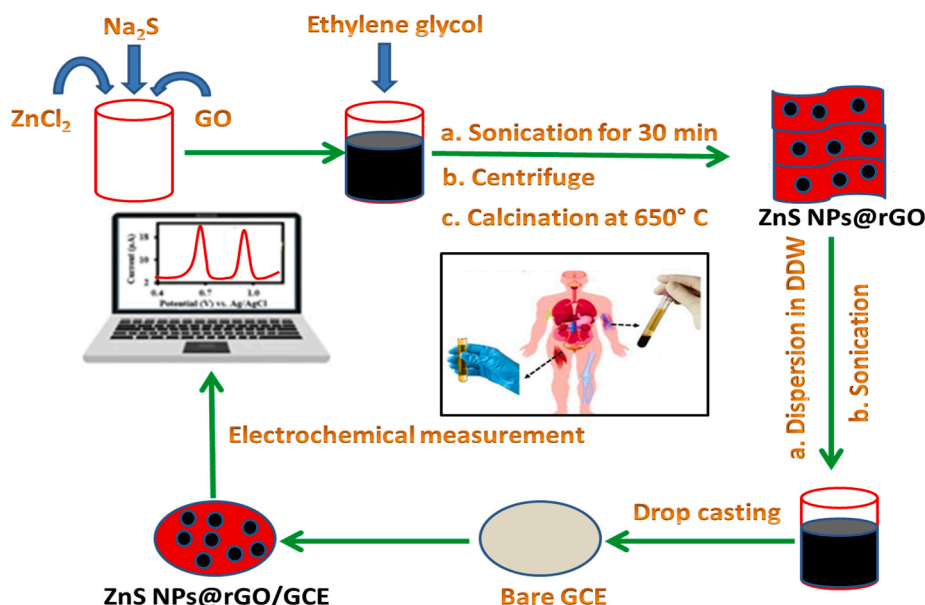
Scheme 1. Representative diagram for preparation of ZnS NPs@rGO/GCE and electrochemical oxidation of HCQ and DAC.

ability and thermal stability [39,40]. Therefore, it has significant applications in various fields including supercapacitors, water splitting reactions, batteries, dye-sensitized solar cells, drug delivery, photo and electro-catalysis [41,42]. Unfortunately, metal sulfides tend to aggregate [43]. As a result, integrating metal sulfides and high conductive matrix into a nanostructure has been demonstrated as a valuable approach to improve the conductivity and non-aggregativity of the nanocomposite [44]. Reduced graphene oxide nanosheets (rGOs) are novel layered materials that possess high conductivity and large electro-catalytic sites or surface areas and have various applications [34,45]. In addition, rGOs are more interacted with metal sulfides and its one kind of electrostatic interaction of two nanomaterials [46,47].

3.3. Morphological and electrochemical characterization of ZnS NPs@rGO

The morphology and composition of ZnS NPs@rGO were investigated using different techniques. Fig. S2a and b show the dispersed particles of ZnS and typical like nanosheets like structure of rGO, respectively. Fig. S2c illustrates the ZnS NPs anchored to the surface of rGO. In addition, the morphologies of ZnS NPs, rGO and ZnS NPs@rGO were confirmed by TEM in Figs. S2(d–f). The size distribution of ZnS NPs was in the range of 25–30 nm. The contents of ZnS NPs@rGO was confirmed by EDX where the main elements in the nanocomposite are carbon (C), oxygen (O), zinc (Zn) and sulfur (S) with percentage amounts of 26.78%, 16.34%, 31.23% and 25.65%, respectively (Fig. S3).

The PXRD results of GO and ZnS NPs@rGO were presented in Fig. S4. The diffraction peak at $11.6°$ corresponds to (0 1 1) plane of the graphene layer spacing d = 0.776 nm [48]. The diffraction peak in ZnS NPs@rGO at $24.6°$ corresponds to (0 0 2) plane of rGO [49–51]. The diffraction peaks at $28.6°$, $33.8°$, $48.2°$, $56.8°$, $59.8°$, $69.3°$ and $76.4°$ correspond to the (1 1 1), (2 0 0), (2 2 0), (3 1 1), (2 2 2), (4 0 0) and (3 3 1) crystalline planes of ZnS, which agree well with JCPDS number 05-0566 [52,53]. Fig. S5 shows the FTIR spectra of pristine graphene oxide nanosheet (GO) and ZnS NPs@rGO. For GO, a broad band at 3420 cm^{-1} that corresponds to δ (OH), while peaks at 1725 cm^{-1}, 1670 cm^{-1}, 1390 cm^{-1}, 1270 cm^{-1} and 1130 cm^{-1} are assigned to δ (C = O), υ (OH), δ (C = C), δ (C-OH), δ (C-O-C), respectively. For ZnS NPs@rGO, The peak at 1725 cm^{-1} for GO is absent for the ZnS NPs@rGO nanocomposite, which indicates the reduction of GO during the ultrasonic irradiation process. Fig. S6 shows the Raman spectra of pristine GO and ZnS NPs@rGO where it shows two main peaks at 1355 cm^{-1} and 1630 cm^{-1}, which correspond to D and G bands, respectively. The D and G bands are assigned to the out-of-plane vibration (A1g symmetry) and in-plane vibration (E2g mode) of sp^2-bonded carbon atoms [54]. In comparison to pristine GO, the Raman spectrum of ZnS NPs@rGO shows ID/IG intensity (1.25) is higher than pristine GO (0.92). Moreover, ZnS NPs@rGO nanocomposite shows small band at 311.5 cm^{-1}, corresponding to Cu-S stretching. The porous structures and surface areas of ZnS NPs and ZnS NPs@rGO nanomaterials were evaluated by BET analysis (Fig. S7). According to IUPAC classification, the isotherms of both exhibited type IV Hysteresis, which indicates mesoporous nature of them [55]. The measured BET surface areas are 14.67 m^2 g^{-1} and 87.67 m^2 g^{-1} for ZnS NPs and ZnS NPs@rGO, respectively.

The electro-catalytic behavior of ZnS NPs@rGO was studied using CV and EIS as seen in Fig. S8. It is obvious that the anodic and cathodic peak currents of 5.0 mM [Fe(CN)$_6$]$^{3-/4-}$ are increased according to the following: unmodified GCE < ZnS NPS/GCE < rGO/GCE < ZnS NPs@rGO/GCE (Fig. S8A). EIS was used to measure Rct at the electrode surface. The Rct values of bare GCE, ZnS NPS, rGO, ZnS NPs@rGO are 657.44, 523.56, 432.10 and 234.57 Ω cm^2, respectively (Fig. S8B). A smaller Rct value was obtained with ZnS NPs@rGO/GCE that means more facile electron transfer and enhanced electro-catalytic activity at the electrode surface. The interaction between ZnS NPs and rGO resulted in enhanced rich anchor sites, structural stability and improved electro-

catalytic performance.

The electrochemical surfaces of bare GCE, ZnS NPS/GCE, rGO/GCE and ZnS NPs@rGO/GCE area were calculated from the voltammetric peak current by use of the Randle-Sevcik equation:

$$Ipa = 2.69 \times 10^5 A D^{1/2} n^{3/2} v^{1/2} C$$

where, Ipa is the anodic peak current. A is the surface area. n is the number of electron involved in redox reaction (n = 1). D is the diffusion coefficient of the molecule in solution (7.6 × 10^{-6} cm^2 s^{-1}). C is the concentration of the probe molecule (5 mM [Fe(CN)$_6$]$^{3-/4-}$). v is the scan rate. From the slope of the Ipc - v$^{1/2}$ relationship, the surface areas of GCE, ZnS NPS/GCE, rGO/GCE and ZnS NPs@rGO/GCE were calculated to be 0.230, 0.441, 0.786 and 1.342 cm^2 (Fig. S9).

3.4. Electrochemical behavior of HCQ and DAC at modified electrodes

The electrochemical behaviors of 50.0 μM of HCQ and DAC on bare GCE (a), ZnS NPS/GCE (b), rGO/GCE (c) and ZnS NPs@rGO/GCE (d) were investigated by CV in B.R. buffer (pH 5.5) (Fig. 1). As shown, there is no redox peaks at the bare GCE and ZnS NPS/GCE. In comparison, well-defined oxidation peaks of DAC and HCQ were obtained at rGO/GCE owing to good conductivity of rGO. For ZnS NPs@rGO/GCE, a larger redox peaks currents were observed. The excellent performance accounts for the synergistic effects of ZnS NPs@rGO/GCE, including the high adsorption capacity, good conductivity, enhanced electron transfer, as well as increase catalytic active sites on the electrode. Furthermore, the interaction mechanisms between HCQ, DAC and ZnS NPs@rGO are in the form of hydrogen bonding (between polar groups of drugs, adsorbed H$_2$O on the surface of ZnS NPs and residual polar groups of rGO) and π-π stacking (between rGO conjugated system and aromatic skeletons of the studied drugs) (Scheme 2).

3.5. Factors governing electrochemical oxidation at ZnS NPs@rGO/GCE

3.5.1. The effect of pH

The electrochemical oxidation of HCQ and DAC at ZnS NPs@rGO/GCE were affected by pH of the medium. The effect of different pH values in the range of 4.5 to 7.0 was investigated and illustrated in Fig. 2. The ZnS NPs@rGO/GCE shows oxidation peaks responses were gradually changed upon increasing the pH value. Markedly, the oxidation peaks potentials of HCQ and DAC were shifted to negative direction upon increasing the pH value, suggesting contribution the protons within the oxidation mechanism [56,57]. In addition, the maximum peak currents for both HCQ and DAC were obtained at pH 5.5. As a result, pH 5.5 was chosen as an optimum value for simultaneous
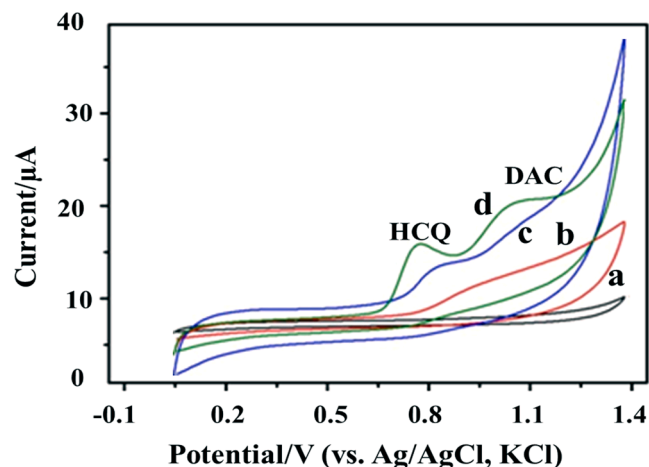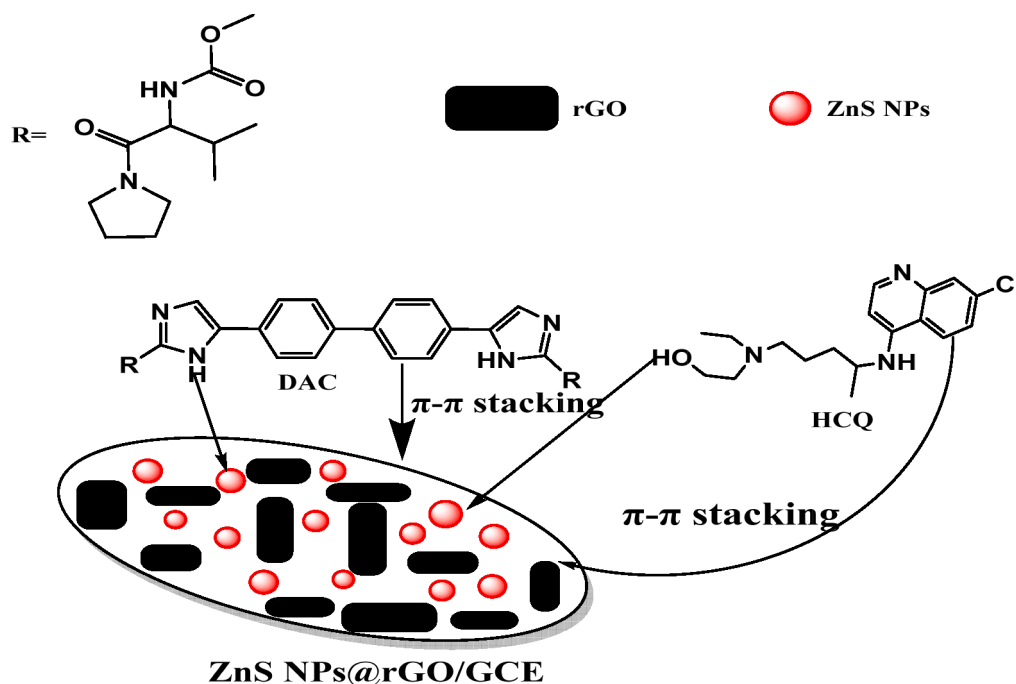

Fig. 1. CVs of 50 μM HCQ and DAC at bare GCE (a), ZnS NPS/GCE (b), rGO/GCE (c) and ZnS NPs@rGO/GCE (d) in B.R. buffer (pH 5.5) at scan rate of 40 mV s^{-1} after preconcentration time of 180 s.

Scheme 2. The interaction mechanisms between DAC, HCQ and ZnS NPs@rGO.
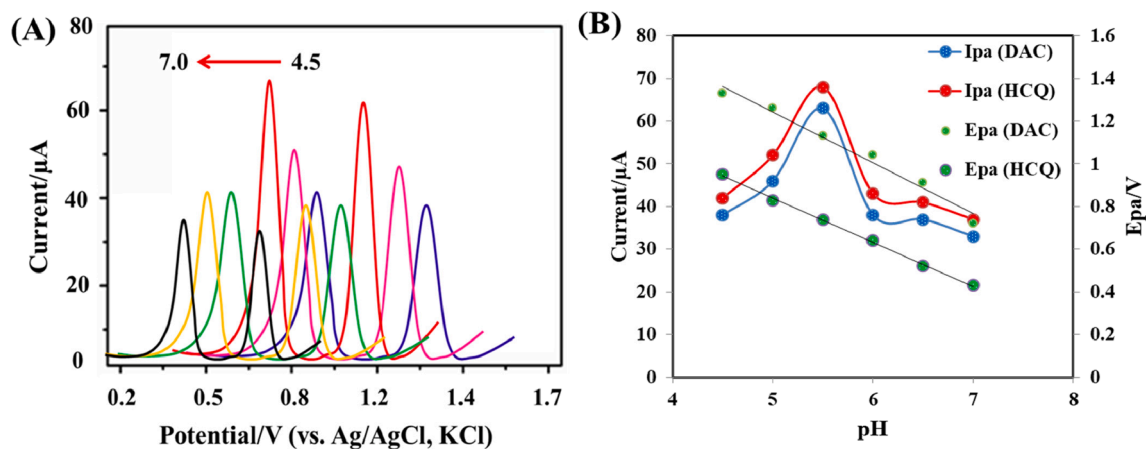

Fig. 2. DPV scans of 10.0 nM HCQ and DAC at ZnS NPs@rGO/GCE.

measurement of HCQ and DAC in their combined mixture. The oxidation peak currents were reduced with increasing pH due to the pKa values of DAC and HCQ, which are 6.09 and 4.0 [58,59]. Moreover, in highly acidic pH ZnS NPs can be oxidized to Zn^{2+}; while in higher pH it can be converted to $Zn(OH)_2$ [60]. As a result, the mechanistic interactions between rGO and ZnS NPs would decrease. Based on these evidences, the pH 5.5 was chosen as an optimum value for simultaneous analysis of DAC and HCQ.

3.5.2. The effect of potential scan rate

Fig. S10A shows the effect of scan rate on the ZnS NPs@rGO/GCE at different scan rate (0.02–0.16 V s^{-1}) in 50 μM HCQ and DAC. The anodic oxidation currents (Ipa) of DAC and HCQ were increased linearly with increasing the scan rate. Fig. S10B exhibits the relationship between the square root of square root of scan rate and Ipa values of DAC and HCQ. The linear regression equations are Ipa (μA) = 22.37 + 480.56 ν (V s-1) (R^2 = 0.9991) and Ipa (μA) = 30.36 + 524.34 ν (V s^{-1}) (R^2 = 0.9991) for HCQ and DAC, respectively. This suggests that the electrochemical oxidation of DAC and HCQ at ZnS NPs@rGO/GCE follow a diffusion

confined process.

3.5.3. DPV conditions

Step height, pulse height, pulse width and pulse period were measured in the range of 0.05–0.5 V, 0.1–0.6 V, 0.01–0.25 V and 0.1–1.0 s. It was found that the optimum conditions for measuring HCQ and DAC are 0.25 V, 0.35 V, 0.15 V and 0.6 s, respectively after deposition time of 150 s.

3.6. Simultaneous electrochemical determination of HCQ and DAC

The ZnS NPs@rGO/GCE combined with DVP under the optimized conditions in B.R. buffer (pH = 5.5). The stripping peaks presented a good peak potential separation (more than 0.35 V), which allows the simultaneous analysis of HCQ and DAC. Initially, the concentration of HCQ was increased linearly in presence of fixed concentration of DAC (Fig. 3A) and vice versa (Fig. 3B).These results confirmed that the change concentration of one compound did not affect the stripping currents of another compound, indicating that their responses are
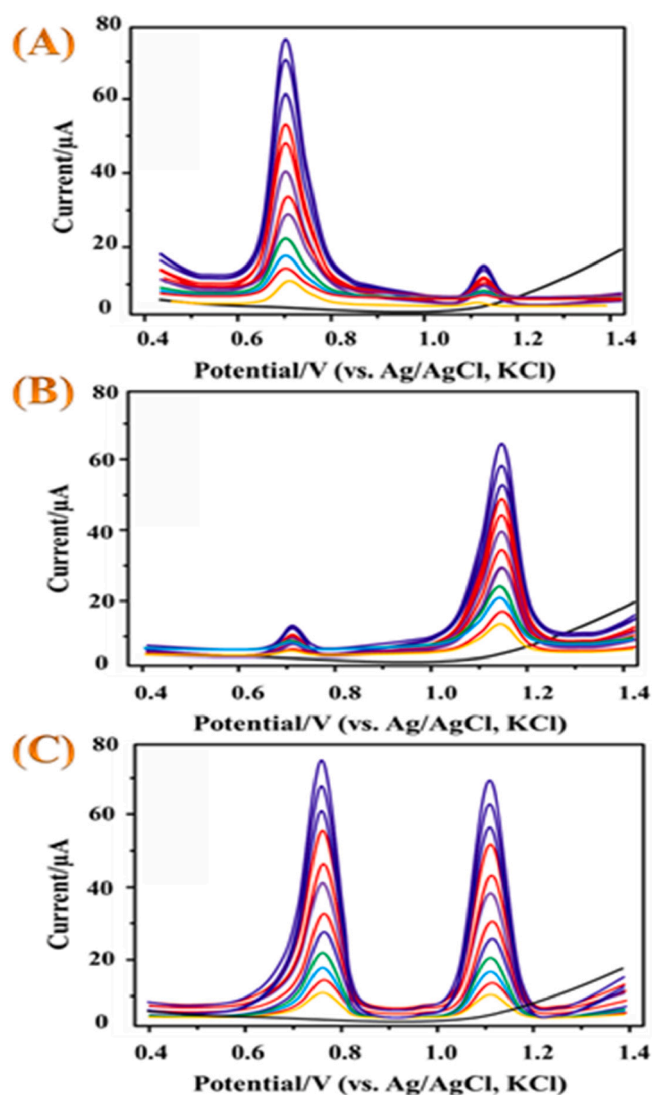
Fig. 3. DPV scans for various concentrations of HCQ (A) and DAC (B) at fixed concentrations of 10.0 nM DAC and 10.0 nM HCQ, respectively. HCQ concentrations (1–12): 5.0–65.0 nM. DAC concentrations (1–12): 7.0–65.0 nM. (C) DPV scans of mixture solution of HCQ and DAC obtained at the modified electrode. At right sides are the corresponding calibration plots. Conditions: Step height, pulse height, pulse width, pulse period and preconcentration time are 0.25 V, 0.35 V, 0.15 V, 0.6 s and 150 s.

independent. Secondly, both HCQ and DAC were determined simultaneously by increasing their concentrations (Fig. 3C). The results of calibration plots were summarized in Table 1. It is clearly observed that

Table 1
Analytical parameters for voltammetric determination of HCQ and DAC obtained at ZnS NPs@rGO/GCE.

Sample	Linear range (nM)	Regression equation	LOQ (nM)	LOD (nM)
(A) HCQ	5.0–65.0	Ipa (µA) = 4.58 + 1.01 C$_{HCQ}$	1.18	0.392
(B) DAC	7.0–65.0	Ipa (µA) = 1.67 + 0.96 C$_{DAC}$	1.15	0.382
(C) HCQ and DAC simultaneously				
HCQ	5.0–65.0	Ipa (µA) = 5.28 + 0.99 C$_{HCQ}$	1.51	0.498
DAC	7.0–65.0	Ipa (µA) = 1.38 + 0.98C$_{DAC}$	1.36	0.456

the values were almost identical for both molecules under optimum conditions of measurement. In addition, the analytical parameters such as linear range and LOD were compared with the previously reported methods for the analysis of HCQ and DAC (Table 2). It can be seen that the proposed electrode has a better electro-catalyst activity than the previously reported methods. Hence, the modified electrode is more suitable for analysis of HCQ and DAC either individually or simultaneously.

3.7. Precision of the proposed method

Reproducibility of the proposed method was studied by measuring the same sample mixture with three different electrodes of the same composition (n = 3). The RSDs % values for HCQ and DAC were found to be 3.5% and 3.2% for HCQ and DAC, respectively. On the other hand, the repeatability was measured by measuring the sample mixture under the same experimental conditions at n = 5 (in the same day) and the RSDs % values were found to be 1.6% and 1.9% for HCQ and DAC, respectively.

3.8. Stability of the modified electrode

The stability of the ZnS NPs@rGO modified GCE was investigated using DPV method at room temperature for simultaneous analysis of HCQ and DAC. The modified electrode retained about 95.89% from its initial activity over 50 cycles (Fig. S11a). This indicates that the modified sensor has good stability due to its content of rGO, which has robust mechanical stability [68]. Moreover, the modified electrode was used for measurement of HCQ and DAC simultaneously for 30 days. It was found that the proposed electrode kept about 96.45% from its initial sensitivity for 25 days (S11b). Furthermore, the stability of the modified electrode was tested before and after analysis and slight variation was seen in the diffraction peaks of ZnS NPs that may be attributed to the oxidation of 2.27% of ZnS to ZnO (Fig. S12).

3.9. Anti-interference study

The effect of potentially interfering compounds such as ascorbic acid (AA), uric acid (UA), glucose (GlC), dopamine (DA), glutathione (GLU), Ca^{2+}, Mg^{2+}, Na$^+$, K$^+$, adenine (Aden), guanine (Gua) and methionine (Meth) was evaluated using 50 nM HCQ and DAC (Fig. S13). It was found that 600 fold of Ca^{2+}, Mg^{2+}, Na$^+$, K$^+$; 450 fold AA, UA, GLC, DA, GLU, Meth; and 400 fold Aden and Gua not affect the anodic potentials and currents of HCQ and DAC (relative errors not exceed 5%). This means that the proposed method can be applied with high reliability for analysis of HCQ and DAC in biological samples.

3.10. Applications of ZnS NPs@rGO/GCE

The analytical applicability of ZnS NPs@rGO/GCE was evaluated by detecting of HCQ and DAC in human plasma and urine samples. The results for detection of HCQ and DAC by standard addition method are cited in Table 3. The samples were analyzed by HPLC method, and it was found that no significant difference between the proposed and HPLC methods. Consequently, the proposed sensor is accurate enough for HCQ and DAC assay in plasma and urine samples.

4. Conclusion(s)

Herein, a simple one pot sonochemical method was proposed for fabrication of ZnS NPs modified rGO. The nanocomposite was characterized using different methods, and used for simultaneous analysis of HCQ and DAC with good selectivity. The ZnS NPs/ rGO showed nanomolar detection of HCQ and DAC with good accuracy and precision. The proposed electrode exhibits some advantages such as high selectivity, sensitivity, reproducibility and stability. The higher electrochemical

Table 2

List of various HCQ and DAC sensors reported vs. ZnS NPs@rGO/GCE.

Electrodes	Technique	Linearity range (nM)	LOD (nM)	Samples	Reference
HCQ					
Bare glassy carbon	DPV	20×10^3-500×10^3	11.2×10^3	Tablets	[61]
Cathodic treated boron diamond	SWV	290–5660	180	Tablets and synthetic urines	[62]
N,N′-bis[(E)-(1-pyridyl) methylidene]-1,3-propanediamine modified GCE	DPV	90–1021	4.5	Human serum	[63]
Schiff′s base modified GCE	DPV	7–11900	4.7	Bulk	[64]
DAC					
Carbon nanotube/nickel nanoparticle/GCE	SWV	24–300×10^3	15.82	Tablet, serum	[65]
Molecularly imprinted polymer/reduced graphene oxide–based carbon-paste sensor	CV	0.04–812	0.012	Plasma and urine	[66]
Chitosan /multi-walled carbon nanotubes and cobalt nanoparticles/ carbon paste electrode	DPV	1–12000	0.88	Tablet, urine and serum	[67]
HCQ and DAC simultaneously					
ZnS NPs@rGO/GCE	DPV	7.0–65.0 (DAC) 5.0–65.0 (HCQ)	0.498(DAC) 0.456 (HCQ)	Plasma and urine	This work

Table 3

Analysis of HCQ and DAC by ZnS NPs@rGO/GCE in human plasma and urine samples (n = 3).

Samples	Added (nM)	Proposed sensor						HPLC method					
		DAC			HCQ			DAC			HCQ		
Plasma 1		Found (nM)	Recovery %±SD	RSD %	Found (nM)	Recovery %±SD	RSD %	Found (nM)	Recovery %±SD	RSD %	Found (nM)	Recovery %±SD	RSD %
	10.0	9.98	99.8 ± 3.12	3.13	9.95	99.5 ± 2.85	2.86	9.87	98.7 ± 4.18	4.23	10.13	101.3 ± 3.98	3.92
	30.0	31.34	104.5 ± 3.87	3.70	30.80	102.7 ± 2.27	2.21	30.34	101.1 ± 5.23	5.17	28.92	96.4 ± 3.86	4.00
Plasma 2													
	15.0	15.08	100.5 ± 2.87	2.87	14.97	99.8 ± 1.89	1.89	14.87	99.1 ± 2.98	3.00	14.92	99.5 ± 4.72	4.74
	40.0	38.78	96.9 ± 3.37	3.48	40.12	100.3 ± 2.49	2.48	40.56	101.4 ± 3.89	3.84	38.87	97.2 ± 3.78	3.88
Urine 1													
	10.0	9.87	98.7 ± 2.95	2.99	10.45	98.7 ± 3.12	3.16	10.15	101.5 ± 2.64	2.60	9.56	95.6 ± 3.34	3.49
	30.0	29.45	98.2 ± 3.51	3.57	30.34	101.1 ± 3.61	3.57	30.67	102.2 ± 3.10	3.06	29.23	97.4 ± 3.87	3.97
Urine 2													
	15.0	15.23	101.5 ± 2.76	2.72	15.27	101.8 ± 3.32	3.26	14.57	97.1 ± 4.78	4.92	15.47	103.1 ± 3.55	3.44
	30.0	30.89	102.9 ± 1.97	1.91	29.65	98.8 ± 2.78	2.81	29.45	98.1 ± 4.67	4.76	30.35	101.1 ± 2.85	2.82

activity of the electrode may be attributed to fast electron transfer, high effective surface area and good conductivity. It was used for determination of the cited drugs in real biological fluids with satisfactory results. Therefore, the ZnS NPs/ rGO modified GCE opens a new venue for its applications as the electrochemical sensor to detect multiple drugs in their matrices.

CRediT authorship contribution statement

Saad A. Alkahtani: Resources, Writing - review & editing. **Ashraf M. Mahmoud:** Investigation, Software, Validation, Visualization, Writing - review & editing. **Mater H. Mahnashi:** Resources, Funding acquisition. **Ali O. AlQarni:** Resources, Writing - review & editing. **Yahya S.A. Alqahtani:** Funding acquisition, Project administration, Resources, Writing - review & editing. **Mohamed M. El-Wekil:** Conceptualization, Data curation, Formal analysis, Investigation, Methodology, Software, Supervision, Validation, Visualization, Writing - original draft, Writing - review & editing.

Declaration of Competing Interest

The authors declare that they have no known competing financial interests or personal relationships that could have appeared to influence the work reported in this paper.

Acknowledgement

Appendix A. Supplementary data

Supplementary data to this article can be found online at https://doi.org/10.1016/j.microc.2021.105972.

References

[1] S. Belouzard, J.K. Millet, B.N. Licitra, G.R. Whittaker, Mechanisms of coronavirus cell entry mediated by the viral spike protein, Viruses 4 (2012) 1011–1033.

[2] A. Walls, M. Tortorici, B. Bosch, et al., Cryo-electron microscopy structure of a coronavirus spike glycoprotein trimer, Nature 531 (2016) 114–117, https://doi.org/10.1038/nature16988.

[3] Y. Yuan, D. Cao, Y. Zhang, et al., Cryo-EM structures of MERS-CoV and SARS-CoV spike glycoproteins reveal the dynamic receptor binding domains, Nat. Commun. 8 (2017) 15092.

[4] B.R. Beck, B. Shin, Y. Choi, S. Park, K. Kang. Predicting commercially available antiviral drugs that may act on the novel coronavirus (2019-nCoV), Wuhan, China through a drug-target interaction deep learning model. https://doi.org/10.1101/2020.01.31.929547. License CC BY-NC-ND 4.0.

[5] T. Mizui, S. Yamashina, I. Tanida, et al., Inhibition of hepatitis C virus replication by chloroquine targeting virus-associated autophagy, J. Gastroenterol. 45 (2010) 195–203, https://doi.org/10.1007/s00535-009-0132-9.

[6] F. Superti, L. Seganti, N. Orsi, et al., The effect of lipophilic amines on the growth of hepatitis A virus in Frp/3 cells, Arch. Virol. 96 (1987) 289–296, https://doi.org/10.1007/BF01320970.

[7] Y. Yan, Z. Zou, Y. Sun, et al., Anti-malaria drug chloroquine is highly effective in treating avian influenza A H5N1 virus infection in an animal model, Cell Res. 23 (2013) 300–302, https://doi.org/10.1038/cr.2012.165.

[8] S.D. Dowall, A. Bosworth, R. Watson, K. Bewley, I. Taylor, E. Rayner, et al., Chloroquine inhibited Ebola virus replication in vitro but failed to protect against infection and disease in the in vivo guinea pig model, J. Gen. Virol. 96 (2015) 3484–3492.

[9] A.H. Koyama, T. Uchida, Inhibition of multiplication of herpes simplex virus type 1 by ammonium chloride and chloroquine, Virology 138 (1984) 332–335.

[10] E.A. Kouroumalis, J. Koskinas, Treatment of chronic active hepatitis B (CAH B) with chloroquine: a preliminary report, Ann. Acad. Med. Singapore 15 (1986) 149–152.

[11] J.J. Kwiek, T.A. Haystead, J. Rudolph, Kinetic mechanism of quinone oxidoreductase 2 and its inhibition by the antimalarial quinolones, Biochemistry 43 (2004) 4538–4547.

[12] M.J. Vincent, E. Bergeron, S. Benjannet, B.R. Erickson, P.E. Rollin, T.G. Ksiazek, et al., Chloroquine is a potent inhibitor of SARS coronavirus infection and spread, Virol. J. 2 (2005) 69, https://doi.org/10.1186/1743-422X-2-69.

[13] J.T. Li, W.Z. Yang, S.X. Wang, S.H. Li, T.S. Li, Improved synthesis of chalcones under ultrasound irradiation, Ultrason. Sonochem. 9 (2002) 237–239.

[14] W. Huang, X. Tang, Y. Wang, Y. Koltypin, A. Gedanken, Selective synthesis of anatase and rutile via ultrasound irradiation, Chem. Commun. 15 (2000) 1415–1416.

[15] K. Dashtian, S. Hajati, M. Ghaedi, L-phenylalanine-imprinted polydopamine-coated CdS/CdSe n-n type II heterojunction as an ultrasensitive photoelectrochemical biosensor for the PKU monitoring, Biosens. Bioelectron. 165 (2020), 112346.

[16] K. Dashtian, S. Hajati, M. Ghaedi, Ti-Based Solid-State Imprinted-Cu2O/CuInSe2 heterojunction photoelectrochemical platform for highly selective dopamine monitoring, Sens. Actuat. B: Chemical 326 (2021), 128824.

[17] K. Dashtian, M. Ghaedi, S. Hajati, Photo-Sensitive Pb5S2I6 crystal incorporated polydopamine biointerface coated on nanoporous TiO2 as an efficient signal-on photoelectrochemical bioassay for ultrasensitive detection of Cr(VI) ions, Biosens. Bioelectron. 132 (2019) 105–114.

[18] F. Amourizi, K. Dashtian, M. Ghaedi, S. Hajati, Colorimetric determination of F-, Br- and I- ions by Ehrlich's bio-reagent oxidation over enzyme mimic like gold nanoparticles: Peroxidase-like activity and multivariate optimization, Spectrochim. Acta Part A Mol. Biomol. Spectrosc. 226 (2020), 117606.

[19] K. Dashtian, R. Zare-Dorabei, Preparation and characterization of a novel optical chemical sensor for determination of trace amounts of Praseodymium ion by UV/Vis spectrophotometry, Sens. Actuat. B: Chemical 242 (2017) 586–594.

[20] F. Amourizi, K. Dashtian, M. Ghaedi, Electrostatically controlled plasmonic effects of gold nanoparticles with indigo-carmine functionation for rapid and straightforward colorimetric detection of Cu2+ ions, Spectrochim. Acta Part A Mol. Biomol. Spectrosc. 230 (2020), 118026.

[21] F. Amourizi, K. Dashtian, M. Ghaedi, Polyvinylalcohol-citrate-stabilized gold nanoparticles supported congo red indicator as an optical sensor for selective colorimetric determination of Cr(III) ion, Polyhedron 176 (2020), 114278.

[22] H.Y. Yea, P.F. Wu, S. Huang, X. Gao, S.S. Song, W.Q. Wang, X.R. Guo, Simultaneous electrochemical determination of levodopa and uric acid based on ZnS nanoparticles/3D graphene foam electrode, Microchem. J. 149 (2019), 103977.

[23] J.W. Suk, R.D. Piner, J. An, R.S. Ruoff, Mechanical properties of monolayer graphene oxide, ACS Nano 4 (2010) 6557–6564.

[24] M. Govindasamy, S. Manavalan, S.-M. Chen, R. Umamaheswari, T.-W. Chen, V. Mani, Determination of oxidative stress biomarker 3-nitro-L-tyrosine using CdWO4 nanodots decorated reduced graphene oxide, Sens. Actuators B 272 (2018) 274–281.

[25] S.M. Chen, R. Umamaheswari, G. Mani, T.-W. Chen, M.A. Ali, A.-H. Fahad, et al., Hierarchically structured CuFe2O4 ND@RGO composite for the detection of oxidative stress biomarker in biological fluids, Inorg. Chem. Front. 5 (2018) 944–950.

[26] U. Rajaji, M. Govindasamy, S.-M. Chen, T.-W. Chen, X. Liu, S. Chinnapaiyan, Microwave-assisted synthesis of Bi2WO6 flowers decorated graphene nanoribbon composite for electrocatalytic sensing of hazardous dihydroxybenzene isomers, Compos. B 152 (2018) 220–230.

[27] M. Govindasamy, R. Umamaheswari, S.-M. Chen, V. Mani, C. Su, Graphene oxide nanoribbons film modified screen-printed carbon electrode for real-time detection of methyl parathion in food samples, J. Electrochem. Soc. 164 (2017) B403–B408.

[28] B. Dinesh, V. Mani, R. Saraswathi, S.M. Chen, Direct electrochemistry of cytochrome c immobilized on a graphene oxide–carbon nanotube composite for picomolar detection of hydrogen peroxide, RSC Adv. 4 (2014) 28229–28237.

[29] V. Mani, R. Devasenathipathy, S.M. Chen, S.F. Wang, P. Devi, Y. Tai, Electrodeposition of copper nanoparticles using pectin scaffold at graphene nanosheets for electrochemical sensing of glucose and hydrogen peroxide, Electrochim. Acta 176 (2015) 804–810.

[30] A.M. Golsheikh, H.N. Lim, R. Zakaria, N.M. Huang, Sonochemical synthesis of reduced graphene oxide uniformly decorated with hierarchical ZnS nanospheres and its enhanced photocatalytic activities, RSC Adv. 5 (2015) 12726–12735.

[31] M. Keerthi, M. Akilarasan, S.-M. Chen, S. Kogularasu, M. Govindasamy, V. Mani, M.A. Ali, F.M. Al-Hemaid, M. Elshikh, One-pot biosynthesis of reduced graphene oxide/prussian blue microcubes composite and its sensitive detection of prophylactic drug dimetridazole, J. Electrochem. Soc. 165 (2018) B27–B33.

[32] V. Mani, B. Devadas, S.M. Chen, Direct electrochemistry of glucose oxidase at electrochemically reduced graphene oxide-multiwalled carbon nanotubes hybrid material modified electrode for glucose biosensor, Biosens. Bioelectron. 41 (2013) 309–315.

[33] S. Manavalan, U. Rajaji, S.-M. Chen, M. Govindasamy, S.S.P. Selvin, T.-W. Chen, M. A. Ali, F.M. Al-Hemaid, M. Elshikh, Sonochemical synthesis of bismuth (III) oxide decorated reduced graphene oxide nanocomposite for detection of hormone (epinephrine) in human and rat serum, Ultrason. Sonochem. 51 (2019) 103–110.

[34] M. Govindasamy, S.F. Wang, S. Kumaravel, R.J. Ramalingam, H.A. Al-lohedan, Facile synthesis of copper sulfide decorated reduced graphene oxide nanocomposite for high sensitive detection of toxic antibiotic in milk, Ultrason. Sonochem. 52 (2018) 382–390.

[35] V. Mani, M. Govindasamy, S.M. Chen, T.W. Chen, A.S. Kumar, S.T. Huang, Core-shell heterostructured multiwalled carbon nanotubes@ reduced graphene oxide nanoribbons/chitosan, a robust nanobiocomposite for enzymatic biosensing of hydrogen peroxide and nitrite, Sci. Rep. 7 (2017) 1–10.

[36] M.M. El-Wekil, A.M. Mahmoud, A.A. Marzouk, S.A. Alkahtani, R. Ali, A novel molecularly imprinted sensing platform based on MWCNTs/AuNPs decorated 3D starfish like hollow nickel skeleton as a highly conductive nanocomposite for selective and ultrasensitive analysis of a novel pan-genotypic inhibitor velpatasvir in body fluids, J. Mol. Liq. 271 (2018) 105–111.

[37] R.L. Stefan, A.J. Szeri, Surfactant scavenging and surface deposition by rising bubbles, J. Colloid Interface Sci. 212 (1999) 1–13.

[38] J.S. McNatt, J.M. Morgan, N. Farkas, R.D. Ramsier, T.L. Young, J. Rapp-Cross, M. P. Espe, T.R. Robinson, L.Y. Nelson, Sonication assisted growth of fluorophosphate films on alumina surfaces, Langmuir 19 (2003) 1148–1153.

[39] H. Liu, D. Su, G. Wang, S.Z. Qiao, An ordered mesoporous WS2 anode material with superior electrochemical performance for lithium ion batteries, J. Mater. Chem. 22 (2012) 17437–17440.

[40] G. Yang, H. Gong, T. Liu, X. Sun, L. Cheng, Z. Liu, Two-dimensional magnetic WS2@ Fe3O4 nanocomposite with mesoporous silica coating for drug delivery and imaging-guided therapy of cancer, Biomaterials 60 (2015) 62–71.

[41] D. Jing, L. Guo, WS2 sensitized mesoporous TiO2 for efficient photocatalytic hydrogen production from water under visible light irradiation, Catal. Commun. 8 (2007) 795–799.

[42] X. Sun, Y. Shi, P. Zhang, C. Zheng, X. Zheng, F. Zhang, Y. Zhang, N. Guan, D. Zhao, G.D. Stucky Container effect in nanocasting synthesis of mesoporous metal oxides. J. Am. Chem. Soc., 133 (2011), pp. 14542-14545.

[43] D.H. Youn, C. Jo, J.Y. Kim, J. Lee, J.S. Lee, Ultrafast synthesis of MoS2 or WS2-reduced graphene oxide composites via hybrid microwave annealing for anode materials of lithium ion batteries, J. Power Sour. 295 (2015) 228–234.

[44] S. Cao, T. Liu, S. Hussain, W. Zeng, X. Peng, F. Pan, Hydrothermal synthesis of variety low dimensional WS2 nanostructures, Mater. Lett. 129 (2014) 205–208.

[45] U. Rajaji, S. Manavalan, S.-M. Chen, M. Govindasamy, T.-W. Chen, T. Maiyalagan, Microwave-assisted synthesis of europium (III) oxide decorated reduced graphene oxide nanocomposite for detection of chloramphenicol in food samples, Compos. Part B: Eng. 161 (2019) 29–36.

[46] V. Mani, M. Govindasamy, S.-M. Chen, T.-W. Chen, A.S. Kumar, S.-T. Huang, Core-shell heterostructured multiwalled carbon nanotubes@ reduced graphene oxide nanoribbons/chitosan, a robust nanobiocomposite for enzymatic biosensing of hydrogen peroxide and nitrite, Sci. Rep. 7 (2017) 11910.

[47] M. Govindasamy, S. Sakthinathan, S.M. Chen, T.W. Chiu, A. Sathiyan, J.P. Merlin, Reduced graphene oxide supported cobalt Bipyridyl complex for sensitive detection of methyl parathion in fruits and vegetables, Electroanalysis 29 (2017) 1950–1960.

[48] Z. Li, X. Wang, Z. Yin, J. Zhao, M. Song, Z. Wu, H. Li, X. Wang, Ag nanoparticles decorated N/S dual-doped graphene nanohybrids for high-performance asymmetric supercapacitors, Carbon 161 (2020) 726–735.

[49] M.M. El-Wekil, A.M. Mahmoud, S.A. Alkahtani, A.A. Marzouk, R. Ali, A facile synthesis of 3D NiFe2O4 nanospheres anchored on a novel ionic liquid modified reduced graphene oxide for electrochemical sensing of ledipasvir: Application to human pharmacokinetic study, Biosens. Bioelectr. 109 (2018) 164–170.

[50] S.A. Alkahtani, A.M. Mahmoud, M.H. Mahnashi, R. Ali, M.M. El-Wekil, Facile fabrication of a novel 3D rose like lanthanum doped zirconia decorated reduced graphene oxide nanosheets: An efficient electro-catalyst for electrochemical reduction of futuristic anti-cancer drug salinomycin during pharmacokinetic study, Biosens. Bioelectr. 150 (2020) 111849.

[51] S.A. Alkahtani, M.M. El-Wekil, A.M. Mahmoud, M.H. Mahnashi, M. Oraby, One pot synthesis of AuPdPt trimetallic nanohybrid decorated reduced graphene oxide nanosheets for ultrasensing of anti-convulsant drug retigabine (ezogabine), J. Electrochem. Soc. 166 (2019) H521–H526.

[52] M.K. Naskar, A. Patra, M. Chatterjee, Understanding the role of surfactants on the preparation of ZnS nanocrystals, J. Colloid Interface Sci. 297 (2006) 271–275.

[53] A.R. Park, K.J. Jeon, C.M. Park, Electrochemical mechanism of Li insertion/extraction in ZnS and ZnS/C anodes for Li-ion batteries, Electrochim. Acta 265 (2018) 107–114.

[54] M.M. El-Wekil, K.K. Abdelhady, R.A. Abdel Salam, G.M. Hadad, R. Ali, Facile synthesis of novel nanocomposite prepared from spinel copper ferrite and reduced graphene oxide in the presence of anti-fouling agent diethyl ammonium acid sulphate for ultrasensitive detection of rosuvastatin in human plasma, Microchem. J. 147 (2019) 1133–1140.

[55] A.M. Mahmoud, S.A. Alkahtani, B.A. Alyami, M.M. El-Wekil, Dual-recognition molecularly imprinted aptasensor based on gold nanoparticles decorated carboxylated carbon nanotubes for highly selective and sensitive determination of histamine in different matrices, Anal. Chim. Acta 1133 (2020) 58–65.

[56] M.H. Mahnashi, A.M. Mahmoud, S.A. Alkahtani, R. Ali, M.M. El-Wekil, Facile fabrication of a novel disposable pencil graphite electrode for simultaneous determination of promising immunosuppressant drugs mycophenolate mofetil and tacrolimus in human biological fluids, Anal. Bioanal. Chem. 412 (2020) 355–364.

[57] F.A. Mohamed, P.Y. Khashaba, R.Y. Shahin, M.M. El-Wekil, A determination approach for rivastigmine by lepidocrocite nanoparticles supported on N-chitosan carbon nanosheets/anti-Fouling PAS: Application to Biosensing, J. Electrochem. Soc. 166 (2019) H41–H46.

[58] R.A. Joghani, A.A. Rafati, J. Ghodsi, P. Assari, A. Feizollahi, A sensitive voltammetric sensor based on carbon nanotube/nickel nanoparticle for determination of daclatasvir (an anti-hepatitis C drug) in real samples, J Appl. Electrochem. 50 (2020) 1199–1208.

[59] R.L. Schroeder, J.P. Gerber, Chloroquine and hydroxychloroquine binding to melanin: Some possible consequences for pathologies, Toxicol. Rep. 1 (2014) 963–968.

[60] M. Wang, Q. Zhang, W. Hao, Z.X. Sun, Surface stoichiometry of zinc sulfide and its effect on the adsorption behaviors of xanthate, Chem. Cent. J. 5 (2011) 73.

[61] M.L.P.M. Arguelho, J.F. Andrade, N.R. Stradiotto, Electrochemical study of hydroxychloroquine and its determination in plaquenil by differential pulse voltammetry, J. Pharm. Biom. Anal. 32 (2003) 269–275.

[62] P.B. Deroco, F.C. Vicentini, G.G. Oliveira, R.C. Rocha-Filho, O. Fatibello-Filho, Square-wave voltammetric determination of hydroxychloroquine in pharmaceutical and synthetic urine samples using a cathodically pretreated boron-doped diamond electrode, J. Electroanal. Chem. 719 (2014) 19–23.

[63] A. Khoobi, S.M. Ghoreishi, M. Behpour, M. Shaterian, M.S. Niasari, Design and evaluation of a highly sensitive nanostructure-based surface modification of glassy carbon electrode for electrochemical studies of hydroxychloroquine in the presence of acetaminophen, Colloids Surf., B 123 (2014) 648–656.

[64] A. Khoobi, S.M. Ghoreishi, M. Behpour, Sensitive and selective determination of hydroxychloroquine in the presence of uric acid using a new nanostructure self-assembled monolayer modified electrode: optimization by multivariate data analysis, Analyst 139 (2014) 4064–4072.

[65] R.A. Joghani, A.A. Rafati, J. Ghodsi, P. Assari, A. Feizollahi, A sensitive voltammetric sensor based on carbon nanotube/nickel nanoparticle for determination of daclatasvir (an anti-hepatitis C drug) in real samples, J. Appl. Electrochem. (2020), https://doi.org/10.1007/s10800-020-01478-1.

[66] N. T. Abdel Ghani, H. Abdulla, M. S. Rizk, A. S. Abo Dena, R. M. El Nashar. Molecularly imprinted polymer/reduced graphene oxide-based carbon-paste sensor for highly sensitive determination of the anti-HCV drug daclatasvir dihydrochloride. Sensors and Actuators B: Chemical 283 (2019) 6–17.

[67] S.M. Azab, A.M. Fekry, Electrochemical design of a new nanosensor based on cobalt nanoparticles, chitosan and MWCNT for the determination of daclatasvir: a hepatitis C antiviral drug, RSC Adv. 7 (2017) 1118–1126.

[68] W. Qin, D. Li, X. Zhang, D. Yan, B. Hu, L. Pan, ZnS nanoparticles embedded in reduced graphene oxide as high performance anode material of sodium-ion batteries, Electrochim. Acta 191 (2016) 435–443.